

Retrieving the real refractive index of mono- and polydisperse colloids from reflectance near the critical angle

Benjamin E. Reed,^{1,*} Roy G. Grainger,² Daniel M. Peters,³ and Andrew J. A. Smith⁴

¹Atmospheric, Oceanic and Planetary Physics, University of Oxford
Clarendon Laboratory, Parks Road, Oxford, OX1 3PU, UK

²COMET, Atmospheric, Oceanic and Planetary Physics, University of Oxford
Clarendon Laboratory, Parks Road, Oxford, OX1 3PU, UK

³now at Rutherford Appleton Laboratory, Didcot, UK

⁴National Centre for Earth Observation. Atmospheric, Oceanic and Planetary Physics,
University of Oxford, Clarendon Laboratory, Parks Road, Oxford, OX1 3PU, UK

*benjamin.reed@physics.ox.ac.uk

Abstract: We investigate the accuracy in retrieving the real refractive index of submicron aerosol particles, at a visible wavelength, from near critical angle reflectance measurements of a dilute suspension of the aerosol. A coherent scattering model (CSM) is used to model the coherent reflectance from the colloidal suspension. We use an extension of the model for polydisperse particles to properly account for the modified size distribution close to the incident medium to colloid interface. We perform a rigorous sensitivity analysis, for both the monodisperse and polydisperse models, to determine how experimental uncertainties propagate into uncertainty in the retrieval of real refractive index. The effect of non-spherical scattering was included in the sensitivity analysis by using T -matrix methods. Experimental reflectance data, at a wavelength of 635 nm, were obtained for monodisperse spherical latex particles, a polydisperse sand sample and a polydisperse volcanic ash sample. We show that the retrieved real refractive index for these particles is consistent with values obtained using other techniques.

© 2016 Optical Society of America

OCIS codes: (010.1110) Aerosols; (290.3030) Index measurements; (290.7050) Turbid media; (120.0120) Instrumentation, measurement, and metrology; (290.0290) Scattering; (290.4020) Mie theory.

References and links

1. P. Forster, V. Ramaswamy, P. Artaxo, T. Bernsten, R. Betts, D. Fahey, J. Haywood, J. Lean, D. Lowe, G. Myhre, J. Nganga, R. Prinn, G. Raga, M. Schulz, and R. V. Dorland, "Changes in atmospheric constituents and in radiative forcing," in *Climate Change 2007: The Physical Science Basis. Contribution of Working Group I to the Fourth assessment report of Intergovernmental Panel on Climate Change*, S. Solomon, D. Qin, M. Manning, Z. Chen, M. Marquis, K. B. Averyt, M. Tignor, and H. L. Miller, eds. (Cambridge University Press, 2007).
2. K. H. Lee, Z. Li, Y. J. Kim, and A. Kokhanovsky, "Atmospheric aerosol monitoring from satellite observations: A history of three decades," in *Atmospheric and Biological Environmental Monitoring* (Springer, 2009).
3. European Commission, *The Impact of the Volcanic Ash Cloud Crisis on the Air Transport Industry* (SEC(2010) 533, 27 April, Brussels., 2010).

4. S. K. Ebmeier, A. M. Sayer, R. G. Grainger, T. A. Mather, and E. Carboni, "Systematic satellite observations of the impact of aerosols from passive volcanic degassing on local cloud properties," *Atmos. Chem. Phys.* **14**, 10601–10618 (2014).
5. C. J. Horwell and P. J. Baxter, "The respiratory health hazards of volcanic ash: a review for volcanic risk mitigation," *Bull. Volcanol.* **69**, 1–24 (2006).
6. R. Blong, *Volcanic Hazards: A Sourcebook on the Effects of Eruptions* (Academic Press, 1984).
7. N. A. Krotkov, D. E. Flittner, A. J. Krueger, A. Kostinski, C. Riley, W. Rose, and O. Torres, "Effect of particle non-sphericity on satellite monitoring of drifting volcanic ash clouds," *J. Quant. Spectrosc. Radiat. Transfer* **63**, 613–630 (1999).
8. E. M. Patterson, "Measurements of the imaginary part of the refractive index between 300 and 700 nanometers for Mount St. Helens ash," *Science* **211**, 836–838 (1981).
9. E. M. Patterson, "Optical absorption coefficients of soil-aerosol particles and volcanic ash between 1 and 16 μm ," *Proceedings of the Second Conference on Atmospheric Radiation* pp. 177–180 (1994).
10. E. M. Patterson, C. O. Pollard, and I. Galindo, "Optical-properties of the ashes from El-Chichon volcano," *Geophys. Res. Lett.* **10**, 317–320 (1983).
11. J. B. Pollack, O. B. Toon, and B. N. Khare, "Optical properties of some terrestrial rocks and glasses," *Icarus* **19**, 372–389 (1973).
12. W. Egan, T. Hilgeman, and K. Pang, "Ultraviolet complex refractive-index of Martian dust — Laboratory measurements of terrestrial analogs," *Icarus* **25**, 344–355 (1975).
13. F. E. Volz, "Infrared optical constants of ammonium sulfate, Sahara dust, volcanic pumice and flyash," *Appl. Optics* **12**, 564–568 (1973).
14. O. B. Toon, J. B. Pollack, and C. Sagan, "Physical properties of the particles composing the Martian dust storm of 1971–1972," *Icarus* **30**, 663–696 (1977).
15. R. G. Grainger, D. M. Peters, G. E. Thomas, A. J. A. Smith, R. Siddans, E. Carboni, and A. Dudhia, *Remote Sensing of Volcanoes and Volcanic Processes: Integrating Observation and Modelling* (Geol. Soc. London Spec. Publ., 2013), vol. 380, chap. Measuring volcanic plume and ash properties from space, pp. 293–320.
16. L. Clarisse, D. Hurtmans, A. J. Prata, F. Karagulian, C. Clerbaux, M. De Maziere, and P.-F. Coheur, "Retrieving radius, concentration, optical depth, and mass of different types of aerosols from high-resolution infrared nadir spectra," *Appl. Optics* **49**, 3713–3722 (2010).
17. G. Gangale, A. J. Prata, and L. Clarisse, "The infrared spectral signature of volcanic ash determined from high-spectral resolution satellite measurements," *Remote Sens. Environ.* **114**, 414–425 (2010).
18. G. E. Thomas, S. F. Bass, R. G. Grainger, and A. Lambert, "Retrieval of aerosol refractive index from extinction spectra with a damped harmonic-oscillator band model," *Appl. Opt.* **44**, 1332–1341 (2005).
19. F. J. K. Becke, "Beziehungen zwischen Dynamometamorphose und Moldkularcolonmen." *Neues Jahrbuch für Mineralogie* pp. 182–183 (1896).
20. L. Kittleman, "Glass-bead silica determination for a suite of volcanic rocks from the Owyee Plateau, Oregon," *Geol. Soc. Am. Bull.* **73** (1963).
21. J. Keller, W. B. F. Ryan, D. Ninkovich, and R. Altherr, "Explosive volcanic activity in the Mediterranean over the past 200,000 yr as recorded in deep-sea sediments," *Geol. Soc. Am. Bull.* **89**, 591–604 (1978).
22. J. G. C. Ball, B. E. Reed, R. G. Grainger, D. M. Peters, T. A. Mather, and D. M. Pyle, "Measurements of the complex refractive index of volcanic ash at 450, 546.7 and 650 nm," *J. Geophys. Res. Atmos.* **120**, 7747–7757 (2015).
23. K. Turnbull, B. Johnson, F. Marenco, J. Haywood, A. Minikin, B. Weinzierl, H. Schlager, U. Schumann, S. Leadbetter, and A. Woolley, "A case study of observations of volcanic ash from the Eyjafjallajökull eruption: 1. In situ airborne observations," *J. Geophys. Res.* **117** (2012).
24. I. Niskanen, J. Räty, and K. Erik Peiponen, "Measurement of refractive index of isotropic particles by incorporating a multifunction spectrophotometer and immersion liquid method," *Appl. Opt.* **46**, 5404–5407 (2007).
25. I. Niskanen and J. R. K. Erik Peiponen, "Determination of the refractive index of microparticles by utilizing light dispersion properties of the particle and an immersion liquid," *Talanta* **115**, 68–73 (2013).
26. R. G. Barrera and A. García-Valenzuela, "Coherent reflectance in a system of random mie scatters and its relation to the effective-medium approach," *J. Opt. Soc. Am. A* **20**, 296–311 (2003).
27. E. Gutiérrez-Reyes, A. García-Valenzuela, and R. G. Barrera, "Overview of an effective-medium approach to the reflection and refraction of light at a turbid colloidal half-space," *Phys. Status Solidi B* **249**, 1140–1147 (2012).
28. R. G. Barrera, A. Reyes-Coronado, and A. García-Valenzuela, "Nonlocal nature of the electrodynamic response of colloidal systems," *Phys. Rev. B* **75**, 184202 (2007).
29. R. G. Barrera, A. García-Valenzuela, C. Sánchez-Pérez, A. Reyes-Coronado, and E. R. Mendez, "Coherent reflection of light from a turbid suspension of particles in an internal reflection configuration: Theory versus experiment," *Opt. Express* **18**, 6724 (2005).
30. A. García-Valenzuela, R. G. Barrera, and E. Gutiérrez-Reyes, "Rigorous theoretical framework for particle sizing in turbid colloids using light refraction," *Opt. Express* **16**, 19741–19756 (2008).
31. A. García-Valenzuela, C. Sánchez-Pérez, and E. Gutiérrez-Reyes, "On the retrieval of particle size from the effective optical properties of colloids," *Physica B* **405**, 3016–3021 (2010).

32. C. Sánchez-Pérez, A. García-Valenzuela, R. Y. Sato-Berrí, J. O. Flores-Flores, and R. G. Barrera, "Sizing colloidal particles from their contribution to the effective refractive index: Experimental results," *J. Phys. Conf. Ser.* **274** (2011).
33. A. García-Valenzuela, C. Sánchez-Pérez, R. G. Barrera, and A. Reyes-Coronado, "Surface Effects on the Coherent Reflection of Light from a Polydisperse Colloid," in *Progress in Electromagnetics Research Symposium 2005* (PIERS Online, 2005), pp. 650–653.
34. M. I. Mishchenko and L. D. Travis, "Capabilities and limitations of a current FORTRAN implementation of the t-matrix method for randomly oriented, rotationally symmetric scatterers," *J. Quant. Spectrosc. Radiat. Transfer* **60**, 309–324 (1998).
35. C. F. Bohren and D. R. Huffman, *Absorption and Scattering of Light by Small Particles* (John Wiley & Sons, 1983).
36. M. I. Mishchenko, J. W. Hovenier, and L. D. Travis, eds., *Light Scattering by Nonspherical Particles: Theory, Measurements and Applications* (Academic Press, 2000).
37. P. Grossel, J. M. Vigoureux, and F. Baïda, "Nonlocal approach to scattering in a one-dimensional problem," *Phys. Rev. A* **50**, 3627–3637 (1994).
38. J. M. Vigoureux, "Use of Einstein's addition law in studies of reflection by stratified planar structures," *J. Opt. Soc. Am. A* **9**, 1313–1319 (1992).
39. C. D. Rodgers, *Inverse Methods for Atmospheric Sounding: Theory and Practice* (World Scientific, 2000).
40. M. Xiaoyan, Q. L. Jun, R. S. Brock, K. M. Jacobs, P. Yang, and X. Hu, "Determination of complex refractive index of polystyrene microspheres from 370 to 1610 nm," *Phys. Med. Biol.* **48**, 4165–4172 (2003).
41. S. N. Kasarova, N. G. Sultanova, C. D. Ivanov, and I. D. Nikolov, "Analysis of the dispersion of optical plastic materials," *Opt. Mater.* **29**, 1481–1490 (2007).

1. Introduction

Measurements of aerosol optical properties are of importance in atmospheric physics because atmospheric aerosols affect the planet's radiative field by scattering and absorbing solar radiation and terrestrial infrared radiation. The interaction of radiation with an aerosol, and the resulting scattering and absorption, is determined by the properties of the aerosol; namely the particle size distribution, shape and complex refractive index. Information about aerosol optical properties is therefore highly relevant for calculations of aerosol radiative forcing needed to predict future climate change [1]. *A priori* information about aerosol optical properties is also needed to fully utilise satellite observations, to retrieve properties such as aerosol optical depth or the columnar concentration of particles [2].

With the Eyjafjallajökull volcanic eruptions of 2010 costing the aviation industry an estimated \$1.7 billion worldwide [3], there is an increasing demand for rapid ash detection and accurate retrieval of ash columnar concentration from satellites, to determine whether airspace is safe for commercial aeroplanes (currently flights are only permitted for ash concentrations less than $2 \times 10^{-3} \text{ g cm}^{-3}$; CAA 2010). Volcanic ash in the stratosphere and troposphere can lead to significant climate perturbations by interacting with solar and infrared radiation as a function of the ash's optical properties, as well as indirectly in the troposphere by acting as cloud condensation nuclei [4]. Additionally there are potential health risks: although high levels of respirable ash ($< 5 \mu\text{m}$ radius) are not known to have serious long term health implications [5], acute respiratory problems are typically reported with ash fallout [6].

For accurate remote sensing of volcanic ash *a priori* information is needed about the complex refractive index of the ash particles, $m_p = n_p + ik_p$. Measurements of volcanic ash refractive indices are limited. Krotkov *et al.* [7] established the complex refractive index of Mt Spurr, Alaska, volcanic ash at three ultraviolet wavelengths. Papers by Patterson *et al.* [8] gave the spectral imaginary refractive index of ash from eruptions of Mt Spurr, Alaska (in the spectral range 0.3–0.7 μm), Mayon (1–16 μm) and El Chichón (0.3–0.7 μm) [8–10]. There are slightly more published data on refractive indices of volcanic materials, such as basalt and andesite [11,12], pumice [13], obsidian [11], and granite [14]. These data show large variation in spectral refractive index between different volcanic rock and ash types [15], and this is reflected in the variability in spectral signatures measured by satellites for different volcanic eruptions [16,17].

This variability necessitates more complete measurements of volcanic ash complex refractive indices from a wide range of volcanic eruptions.

Recently progress has been made by Grainger *et al.* [15] who retrieved the complex refractive index of ash, in the spectral range 1–20 μm , from the Mt Aso, Japan, eruption of 1993. The retrieval technique, outlined in [18] Thomas *et al.*, used to obtain the spectral complex refractive index from transmission cell measurements of the suspended ash requires *a priori* knowledge of the shortwave real refractive index of the ash. This, in part, motivates the development of the technique, presented in this paper, which enables determination of the real refractive index in the visible of submicron polydisperse aerosol samples. The real refractive index in the visible of any aerosol is also useful independently, in order to determine how the aerosol scatters solar radiation in the atmosphere.

The Becke line test [19] is a well established technique involving the use of an optical microscope to determine the relative real refractive index of two materials. The method has been widely used to determine the real refractive index in the visible of volcanic rock, e.g. [20] Kitteman *et al.* and glass dominated volcanic ash, e.g. [21] Keller *et al.* Recently the method was extended to allow determination of the imaginary refractive index of volcanic ash samples: the paper [22] presents results of the complex refractive index at three different wavelengths in the visible for a range of volcanic ashes from different eruptions. However, microscopic techniques are limited by the resolving power of the microscope and can typically only be applied to particles with a diameter $> 1 \mu\text{m}$. The advantage of the technique outlined here is its sensitivity to submicron particles. Submicron ash particles have longer atmospheric lifetimes and were shown, for example, to dominate (by number) the size distribution of the ash cloud from the May 2010 Eyjafjallajökull eruption [23].

Good accuracy in retrieving the real refractive index of powders has been achieved using transmission measurements with the immersion liquid method [24, 25] and can be applied to submicron particles. However, a disadvantage of this method is that it requires many repeat experiments in multiple immersion liquids, which may be difficult when only a very small quantity of a unique sample is available. An advantage of the method we present is it has the ability to retrieve information about the size distribution in addition to the real refractive index of the sample.

This paper outlines a technique for retrieving the real refractive index of monodisperse and polydisperse submicron particles from angular reflectance measurements, close to the critical angle, of a colloidal suspension of particles. In order to model the reflectivity from such a system we use an extended effective medium approach called the coherent scattering model (CSM) developed by Barrera and García-Valenzuela [26] and summarised further in [27], Reyes *et al.* Wave-scattering theory is used in [26] to calculate the coherent reflection from a half-space of scatterers and it is shown that the derived reflectivity is consistent with continuum electrodynamics, providing the effective medium possesses both an effective dielectric response ϵ^{eff} and an effective magnetic susceptibility μ^{eff} . The electrodynamic response of colloids has been shown to be nonlocal in nature [28]; the derived effective responses presented in [26] depend on the angle of the incident wavevector. The model has been shown to be consistent with experimental reflectance data [29], in an experimental set-up very similar to the one we use. Experiments have also been performed, using similar theories, with a focus on determining the size of particles [30–32].

The apparatus and experimental method are presented in section 2. A summary of the theory is presented in section 3. An extension of the model for polydisperse particles, along similar lines to that by García-Valenzuela *et al.* [33], is presented to properly account for the modified size distribution close to the medium-to-colloid interface, which occurs as a result of a higher relative density of smaller particles close to the interface. In section 4, the results of

a sensitivity analysis of the forward model for the monodisperse and polydisperse cases are presented, determining how experimental uncertainties propagate into uncertainty associated with the retrieval of real refractive index. The effect of non-spherical scattering was included in the sensitivity analysis by using *T*-matrix methods [34]. Section 5 presents the retrieval results performed on experimental reflectance data obtained for a monodisperse suspension of polystyrene latex spheres, a polydisperse sand sample and a polydisperse volcanic ash sample. Concluding remarks are made in section 6.

2. The experimental apparatus and methods

2.1. Overview of the apparatus

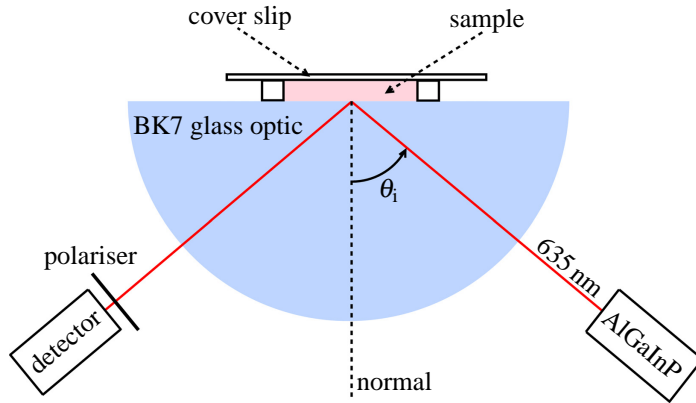


Fig. 1. Schematic of the experimental setup. The 635 nm incident beam from the AlGaInP laser diode enters the optic at normal incidence. It is then reflected at the back surface of the optic at the interface with the sample medium, before exiting the optic and travelling to the detector.

The apparatus is designed to measure the reflectance as a function of incidence angle, θ_i , about an interface between an incident medium and a colloid. The experimental setup is illustrated in Fig. 1. An AlGaInP laser diode produces a collimated beam of light ($\lambda_0 = 635$ nm) which enters a semicircular BK7 glass optic at normal incidence to the curved surface. The refractive index of the glass optic is $n = 1.515$ at the laser wavelength. The beam is then incident on the back surface of the optic at the interface with the sample medium. The coherent component of the reflected beam exits the optic in the specular direction at normal incidence to the curved surface, and travels to a silicon photodetector.

The laser diode and detector are mounted on the arms of a goniometer driven by a stepper motor, and can rotate fully about the optic. The centre of rotation of the arms is aligned with the centre of curvature of the optic, ensuring the beam enters and exits the optic at normal incidence to the curved surface. The setup allows capture of reflectance for a full range of incidence angles ($0^\circ \leq \theta_i \leq 90^\circ$) with a minimum angular interval, determined by the stepper motor, of $\Delta\theta_i = 0.3^\circ$.

The angular positions of the laser and detector arms of the goniometer were controlled by a microcontroller, allowing an automated scanning routine to be pre-programmed. For a typical reflectance scan, the laser and detector were rotated in synchronisation, such that the detector remained aligned along the specular direction as θ_i varied.

In all of the reflectance scans performed, a polarising filter was placed in front of the detector and aligned such that the only light reaching the detector was the component with the *E*-field perpendicularly polarised (\perp) with respect to the plane of incidence (the plane of incidence is

the plane containing the incident wavevector and the vector normal to the reflecting surface). The incident laser beam was unpolarised.

Before tests were performed on colloidal samples, the accuracy of the apparatus was tested by performing reflectance scans on distilled water (the refractive index of which is known to high accuracy). The goniometer allows the incidence angle, θ_i , to be measured with an uncertainty of 0.1° . The uncertainty in the laser power over the duration of a typical reflectance scan was found to be approximately 1%. The reflectance data recorded for distilled water was used (employing Fresnel reflectance theory) to accurately obtain its refractive index to within 0.1%, in agreement with error propagation estimates.

Tests were performed on three aerosol types: spherical polystyrene test particles, a commercial sand sample and a volcanic ash sample. The correct preparation of samples was crucial to obtain reliable reflectance data. Proper dispersal of the aerosol particles in the suspension liquid was required. In all cases ultrasonic vibration was used immediately before reflectance scans were performed in order to evenly disperse the sample in the suspension liquid. In addition, an ultrasonic vibrator was attached to the optic and used throughout scans to maintain uniform dispersal.

2.2. Method: Monodisperse polystyrene latex test particles

Reflectance measurements were performed on colloids containing polystyrene latex spherical beads produced by Sigma-Aldrich UK. The sample supplied by the manufacturer was quoted to contain a fraction of $10.0 \pm 0.5\%$ w/w latex to water and between 0.3 to 1.5% of a soluble polymer dispersant (used to stabilise the particles against flocculation and agglomeration). The sample was manufactured to be monodisperse, with a quoted particle radius of $a = 260\text{ nm}$ and a quoted coefficient of variation in size of $\leq 3\%$.

Diluted samples were produced by adding a measured mass of distilled water to a measured quantity of the $10.0 \pm 0.5\%$ w/w sample. Scales accurate to 0.0001 g were used for sample preparation, with a typical diluted sample having a mass of $\sim 1\text{ g}$. It was therefore possible to determine the volume filling fraction of the diluted samples (the volume filling fraction of a particular constituent in a mixture is defined as the ratio of the volume of the constituent to the total volume of the mixture) to within $\pm 5\%$ resulting from the uncertainty associated with the undiluted sample's mass fraction.

The undiluted sample was placed in an ultrasonic bath for 15 seconds before dilutions were made, to ensure proper dispersal of the polystyrene beads. It was found that the diluted samples required a longer period of 3 minutes in the ultrasonic bath to ensure proper dispersal (determined by eye) possibly due to a reduction in the concentration of the soluble polymer dispersant.

Reflectance scans were performed on polystyrene latex sphere suspensions in distilled water at five different volume filling fractions up to a maximum value of $f = 10.3\%$.

2.3. Method: polydisperse sand sample

A commercial sand sample was used to test the application to a polydisperse sample with an expected uniform composition with particle size. The results of a sensitivity analysis, shown in section 4, performed on the polydisperse CSM assuming a lognormal distribution indicate that uncertainty in the retrieval of refractive index has a minimum for a size parameter of approximately 1.9, and the uncertainty increases with increasing size parameter. For a laser wavelength of 635 nm, a size parameter of 1.9 corresponds to a modal radius of approximately 190 nm. It is therefore necessary, for a typical sand or volcanic ash sample, to separate the fine fraction from the bulk. A sedimentation process was applied for this purpose.

In preparation of the sample used for reflectance scans, approximately 100 grams of the orig-

inal sand sample was dispersed in the 900 ml of distilled water, and left to settle for 24 hours. After this period, with only a fine fraction of sand particles remaining in suspension, the suspension was drawn off from the sedimented fallout. This suspension of fine sand was then condensed down by gentle heating such that water was lost by evaporation.

It was then necessary to condense down the sample to the extent that the volume filling fraction of the sand was sufficiently high so as to produce a significant reflectance signal (i.e. a reflectance curve differing sufficiently from that of distilled water, due to the scattering effect of sand particles). An iterative process was adopted: A reflectance scan was performed using approximately 3 ml of the sample and the reflectance curve was plotted and compared to the reflectance curve of distilled water; then depending on the strength of the signal, the sample was further condensed. This process was repeated until the reflectance signal was judged to be sufficiently high so as to give an accurate retrieval.

Once the reflectance signal was sufficiently high (and the retrieval performed on the data indicated a volume filling fraction $> 3\%$) repeated scans were performed whilst incrementally increasing the concentration of particles to give a range of volume filling fractions.

2.4. Method: polydisperse ash sample

A commercially purchased sample of fine Icelandic volcanic ash, of unverified origin, was used to verify the technique. The method adopted for the ash sample was similar to that used for the sand sample. The exception being that the bulk mass of the ash sample available for experiments was considerably less. The same ratio of distilled water to bulk sample was used for the sedimentation process, using a mass of 20 grams of ash. Two samples were produced in this way; one was allowed to settle for 12 hours (sample A) whilst the period for the second was 24 hours (sample B).

A similar process, as outlined in section 2.3, was applied to condense down the sample to a high enough ash volume filling fraction to achieve suitable reflectance data.

3. Theory

A forward model, \mathbf{F} , is required that relates the measured reflectance as a function of incidence angle to the optical properties of the particles, principally their real refractive index, n_p . The model chosen for this purpose was the coherent scattering model (CSM) outlined in [26].

3.1. The scattering amplitude matrix

Following [35], for a plane wave with an electric field of the form $\mathbf{E}_i = \mathbf{E}_{0i} \exp(i\mathbf{k}_i \cdot \mathbf{r} - i\omega t)$ incident on an arbitrary particle at the origin the relationship between the scattered far field and incident field is:

$$\begin{pmatrix} E_{\parallel}^S \\ E_{\perp}^S \end{pmatrix} = \frac{\exp(ikr)}{-ikr} \begin{bmatrix} S_2(\theta) & S_4(\theta) \\ S_3(\theta) & S_1(\theta) \end{bmatrix} \begin{pmatrix} E_{\parallel}^i \\ E_{\perp}^i \end{pmatrix} \quad (1)$$

where the subscripts \parallel and \perp denote parallel and perpendicular, respectively, with respect to the scattering plane, which is the plane containing the incident and scattered wave vectors, and where θ is the scattering angle between the two wave vectors.

For a spherical particle, $S_3(\theta) = S_4(\theta) = 0$. This condition also holds for the configurationally averaged scattering amplitude functions of non-spherical particles randomly orientated in an isotropic medium [36].

3.2. The Fresnel equations

The Fresnel equations describe the reflectivity at an interface between two homogeneous media: an incident medium and a transmission medium. In the derivation of these equations it is

assumed that the transmission medium extends infinitely beyond the interface, such that there is no additional component to the reflectivity arising from reflection at a second interface; The Fresnel reflectivity amplitudes are therefore half space reflectivity amplitudes for homogeneous media. The expressions for the reflectivity coefficient for the E -field polarised perpendicular (\perp) to the plane of incidence and for the E -field parallel (\parallel) to the plane of incidence may be written in terms of the complex permittivity ϵ and complex permeability μ of the two media:

$$r_{\perp}^{\text{Fres}} = \left(\frac{E_r}{E_i} \right)_{\perp} = \frac{\mu_t n_i \cos(\theta_i) - \mu_i n_t \cos(\theta_t)}{\mu_t n_i \cos(\theta_i) + \mu_i n_t \cos(\theta_t)}, \quad r_{\parallel}^{\text{Fres}} = \left(\frac{E_r}{E_i} \right)_{\parallel} = \frac{\epsilon_t n_i \cos(\theta_i) - \epsilon_i n_t \cos(\theta_t)}{\epsilon_t n_i \cos(\theta_i) + \epsilon_i n_t \cos(\theta_t)}, \quad (2)$$

where the subscripts i, r and t refer to the incident, reflected and transmitted rays respectively. Knowledge of the complex refractive index:

$$n = \sqrt{\epsilon \mu / \mu_0 \epsilon_0}, \quad (3)$$

is insufficient to determine the interface reflectivity: μ and ϵ must be known individually. The exception being materials with no magnetic response, such that $\mu = \mu_0$ and $n = \sqrt{\epsilon / \epsilon_0}$, where knowledge of n is sufficient. The reflectivity r is related to the reflectance R (the ratio of the reflected intensity to the incident intensity; the quantity measured by a detector) according to $R = |r|^2$.

3.3. N -layered slab system

Consider the case of a general N -layered system depicted in Fig. 2. The z -direction is defined to be perpendicular to the slab interfaces, with positive z going rightwards in Fig. 2. Using the composition law of amplitude [37, 38], the reflectivity coefficient at the first interface $\Gamma_{0,1}$ can be expressed as:

$$\Gamma_{0,1}(\theta_0) = \frac{r_{0,1}^{\text{hs}}(\theta_0) + \Gamma_{1,2}(\theta_1) \exp(2ik_1^z \Delta z_1)}{1 + r_{0,1}^{\text{hs}}(\theta_0) \Gamma_{1,2}(\theta_1) \exp(2ik_1^z \Delta z_1)}, \quad (4)$$

where $\Gamma_{1,2}(\theta_1)$ is the reflectivity coefficient for light in medium 1 incident at angle θ_1 on the interface with medium 2. The term $r_{0,1}^{\text{hs}}(\theta_0)$ is a half space reflectivity: it is the reflectivity at the interface $0 \rightarrow 1$ if medium 1 were to extend infinitely beyond the interface; removing all other interfaces the equation simplifies to: $\Gamma_{0,1}(\theta_0) = r_{0,1}^{\text{hs}}(\theta_0)$. Equation (4) can be readily generalised to give the reflectivity coefficient of light in slab m incident on the interface with slab $(m+1)$:

$$\Gamma_{m,m+1}(\theta_m) = \frac{r_{m,m+1}^{\text{hs}}(\theta_m) + \Gamma_{m+1,m+2}(\theta_{m+1}) \exp(2ik_{m+1}^z \Delta z_{m+1})}{1 + r_{m,m+1}^{\text{hs}}(\theta_m) \Gamma_{m+1,m+2}(\theta_{m+1}) \exp(2ik_{m+1}^z \Delta z_{m+1})}, \quad (5)$$

where k_m^z is the z -component of the wavevector of light in medium m , such that $k_m^z = k_m \cos \theta_m$ and where $k_m = 2\pi/\lambda_m$ is the wave number in medium m . The width of slab m is Δz_m . The angle θ_m of light with respect to the z -axis in medium m can be calculated for a given system incidence angle θ_0 by m successive applications of Snell's law:

$$\theta_m = \sin^{-1} \left(\frac{n_{m-1}}{n_m} \sin \theta_{m-1} \right). \quad (6)$$

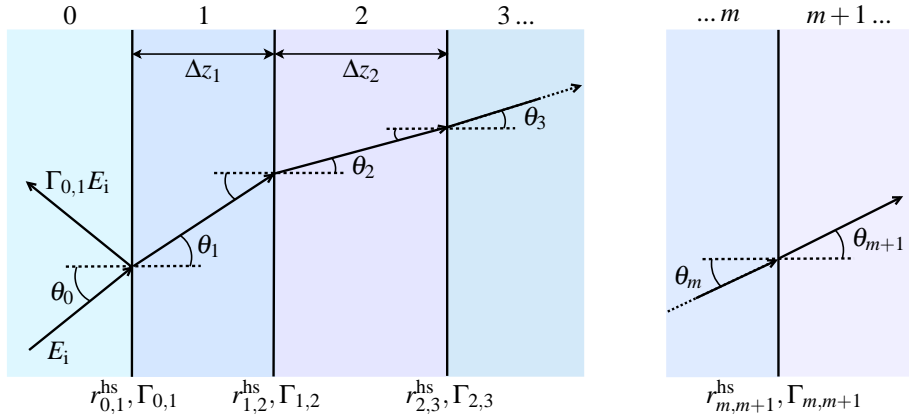


Fig. 2. Reflectivity from an N -layered system of slabs. Only the penetrating beam is shown after the initial interface. The compound reflectivity at the initial interface, $\Gamma_{0,1}$, has a component from reflectivity at each subsequent interface according to Eq. (5).

3.4. The coherent scattering model (CSM) and the effective optical properties of a colloidal system

As outlined in [26], taking into account the Mie scattering of particles, it is possible to determine an effective electric permittivity ϵ^{eff} and magnetic permeability μ^{eff} for a dilute system of random spheres that describe the propagation of the coherent beam. These derived optical coefficients are not continuous functions of space, but depend on the angle of light with respect to the z -axis and the light's polarisation. When ϵ^{eff} and μ^{eff} are substituted into Eq. (2), employing Eq. (3), an expression for the reflectivity of a half space of dilute random spheres is established. We note that the half space reflectivity is derived from wave scattering theory and does not rely on the interpretation of the system as an effective medium. The effective optical coefficients depend on the Mie scattering amplitude functions $S_j(\theta, x, m_p/m_m)$ as defined in [35], where $j = 1$ is employed for \perp polarised light and $j = 2$ for \parallel polarised light. The Mie scattering amplitude functions depend on the ratio of the complex refractive index of the particles to the complex refractive index of the surrounding medium, m_p/m_m . In the retrievals presented in this paper, it is assumed that the particles are non-absorbing (the uncertainty associated with retrievals of n_p arising from assuming $k_p = 0$ is shown to be negligible in section 4) and the suspension medium is non-absorbing, so that $m_p/m_m = n_p/n_m$. The Mie scattering amplitude functions also depend on the size parameter of particles: $x = 2\pi a/\lambda_m$, where $\lambda_m = n_m/\lambda_0$ is the wavelength of light in the suspension medium and λ_0 is the vacuum laser wavelength. The effective optical properties for \perp polarised incident light are:

$$\frac{\mu_{\perp}^{\text{eff}}}{\mu_0} = 1 + i\gamma \frac{S_{-}^{(1)}(\theta_i)}{\cos^2 \theta_i}, \quad (7)$$

$$\frac{\epsilon_{\perp}^{\text{eff}}}{\epsilon_0} = 1 + i\gamma \left[2S_{+}^{(1)}(\theta_i) - S_{-}^{(1)}(\theta_i) \tan^2 \theta_i \right], \quad (8)$$

where

$$S_{+}^{(j)}(\theta_i) = \frac{1}{2} [S(0) + S_j(\pi - 2\theta_i)], \quad (9)$$

$$S_{-}^{(j)}(\theta_i) = S(\theta_i) - S_j(\pi - 2\theta_i). \quad (10)$$

Here $\gamma = 3f/2x^3$, and f is the volume filling fraction occupied by the particles.

For \parallel polarised incident light, the corresponding expressions are:

$$\frac{\epsilon_{\parallel}^{\text{eff}}}{\epsilon_0} = 1 + i\gamma \frac{S_{-}^{(2)}(\theta_i)}{\cos^2 \theta_i}, \quad (11)$$

$$\frac{\mu_{\parallel}^{\text{eff}}}{\mu_0} = 1 + i\gamma \left[2S_{+}^{(2)}(\theta_i) - S_{-}^{(2)}(\theta_i) \tan^2 \theta_i \right]. \quad (12)$$

Substitution of Eqs. (7) and (8) for \perp polarised light or Eqs. (11) and (12) for \parallel polarised light into Eq. (2) yields Eq. (13) an expression for the reflection coefficient for a half space of random particles r_{hs} , as depicted in Fig. 3(a). The centres of the particles lie in the region $z > 0$ but due to the finite size of the particles some protrude into the region $z < 0$. The expression for the half space reflection coefficient is:

$$r_{hs}^{\text{eff}}(\theta_i) = \frac{\gamma S_j(\pi - 2\theta_i) / \cos \theta_i}{i \left(\cos \theta_i + \left\{ \cos^2 \theta_i + 2i\gamma S(0) - \frac{\gamma^2}{\cos^2 \theta_i} [S(0)^2 - S_j(\pi - 2\theta_i)^2] \right\}^{1/2} \right) - \frac{\gamma S(0)}{\cos \theta_i}} \quad (13)$$

where $j = 1$ for \perp polarised incident light and $j = 2$ for \parallel polarised light.

The z -component of the wavevector of the coherent beam in the scattering medium k_z^{eff} is given by:

$$k_z^{\text{eff}} = \sqrt{(k_m^z)^2 - 2i\chi S(0) k_m^z / \cos \theta_i + (\chi^2 / \cos^2 \theta_i) [S_j(\pi - 2\theta_i)^2 - S(0)^2]} \quad (14)$$

where $\chi = -3f/2a^3k_m^2$ and a is the particle radius. We note that Eqs. (13) and (14) are derived from a wave-scattering approach, and do not rely on the interpretation of the system as an effective medium [26, 27].

Now consider the case of an interface (located at $z = 0$) between an incident medium ($z < 0$) and a turbid medium ($z > 0$) containing randomly located spheres with a dilute concentration, as depicted in Fig. 3(b). Given the condition that no particles in the turbid medium may protrude into the incident medium, the centres of all particles must lie in the region $z > a$. Thus there exists an excluded slab of width $\Delta z = a$ in which the centres of particles may not lie and application of Eq. (4) yields the interface reflectivity:

$$r = \frac{r_{i,m}^{\text{Fres}} + r_{hs}^{\text{eff}}(\theta_m) \exp(2ik_m^z a)}{1 + r_{i,m}^{\text{Fres}} r_{hs}^{\text{eff}}(\theta_m) \exp(2ik_m^z a)}, \quad (15)$$

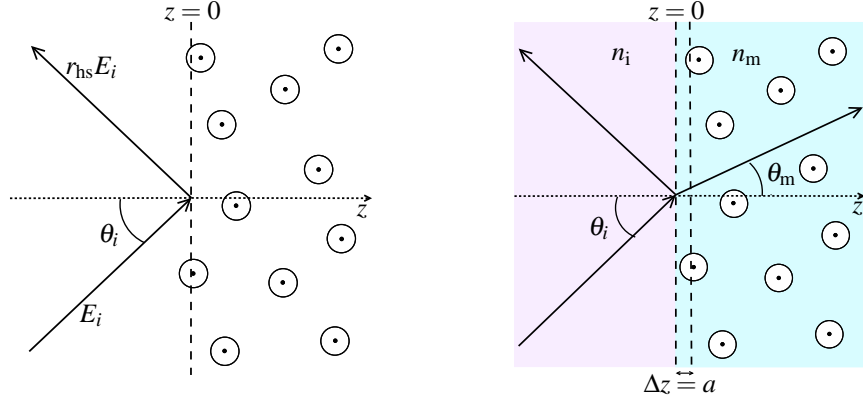
where $r_{i,m}^{\text{Fres}}$ is the Fresnel reflectivity for an interface between a homogeneous medium with refractive index n_i and a homogeneous medium with refractive index n_m .

3.5. Polydisperse systems

The expressions for the optical coefficients are easily modified to account for polydisperse particle size distributions. The amplitude scattering function $S_j(\theta, a)$, in Eqs. (7), (8), (11) and (12), is replaced by an average value integrated over the size distribution: $\int_0^{\infty} S_j(\theta, a) n(a) da$,

where $n(a)$ is the normalised size distribution function (such that $\int_0^{\infty} n(a) da = 1$).

As outlined in [29], an additional complication arises when modelling the reflectivity at an interface between an incident medium and a turbid medium containing a random dilute system



(a) Reflectivity from a half space of spheres.

(b) Reflectivity at an interface between an incident medium and a turbid medium containing randomly located spheres.

Fig. 3. Reflectivity from two systems containing random spheres.

of polydisperse particles: A particle of radius a cannot approach closer than a to the interface, resulting in the relative density of smaller particles increasing as the interface is approached. Thus the size distribution close to the interface is modified according to:

$$n(a, z) = U(z - a)n(a), \quad (16)$$

where $U(x)$ is a step function defined by: $U(x) = 0$ for $x < 0$, and $U(x) = 1$ for $x \geq 0$. Sufficiently far from the interface, the distribution is described by the unmodified distribution $n(a)$.

In order to model the coherent reflectivity from a polydisperse colloid, the system can be split into three parts: the incident medium at $z < 0$; a transition region inside the colloid consisting of N slabs of equal width Δz extending from $z = 0$ to $z = N\Delta z$; and finally a region with the unmodified bulk distribution $n(a)$ occupying $z > N\Delta z$. In the model approximation, within the transition region, the size distribution of particles is assumed to be constant within each slab but varies between slabs. Figure 4 demonstrates how the particle size distribution in slab m of the transition region is restricted to particles with radius $a < m\Delta z$. Such a system provides an approximation that tends to the modified distribution described by Eq. (16) as Δz becomes small and N large.

In order to determine the reflectivity from the approximate model system depicted in Fig. 4, Eqs. (7) and (8) or (11) and (12) (depending on the polarisation) must be used to establish the effective optical properties of each slab, integrating the amplitude scattering function $S_j(\theta, a)$ over the appropriately truncated particle size distribution. For slab m the appropriate replacement being: $\int_0^{m\Delta z} S_j(\theta, a)n(a)da$. In the region $z > N\Delta z$ the appropriate replacement is

the integral over the entire distribution: $\int_0^{\infty} S_j(\theta, a)n(a)da$.

Once the effective optical properties of each region of the approximate model system have been established, the system reflectivity Γ_{01} can be readily calculated using successive applications of Eq. (5). In the retrievals performed on the polydisperse volcanic ash and the polydisperse sand sample, a lognormal distribution was assumed with a median radius, a_0 , and a geometric standard deviation, S :

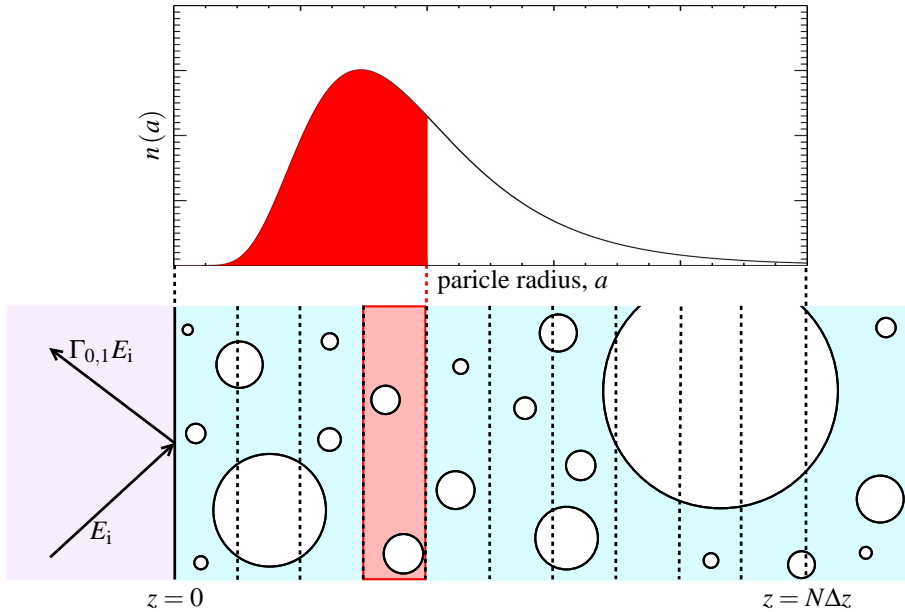


Fig. 4. Illustration of modelling the reflectivity from a polydisperse colloid, using an N -slab transition region extending from $z = 0$ to $z = N\Delta z$. The diagram illustrates how in slab m the distribution of particles is restricted to those with radius $a < m\Delta z$.

$$n(a) = \frac{1}{\sqrt{2\pi} \ln(S)} a \exp \left[\frac{\ln(a) - \ln(a_0)}{2 \ln^2(S)} \right]. \quad (17)$$

4. Sensitivity analysis

In order to determine how measurement errors and other errors propagate through the forward model into uncertainty associated with the retrieved real refractive index n_p , a sensitivity analysis was performed for the monodisperse model and the polydisperse model.

4.1. Error propagation formalism

We follow the error analysis formalism outlined in [39]. For the general problem, the measurement vector, \mathbf{y} , is related to the state vector, \mathbf{x} , and the measurement error, $\boldsymbol{\epsilon}$, via:

$$\mathbf{y} = \mathbf{F}(\mathbf{x}, \mathbf{b}) + \boldsymbol{\epsilon}, \quad (18)$$

where $\mathbf{F}(\mathbf{x}, \mathbf{b})$ is the forward model, and \mathbf{b} is the set of assumed forward model parameters. In this application, the measurement vector \mathbf{y} contains the set of m detector readings recorded for the specularly reflected beam at m values of the incidence angle θ_i . The state vector \mathbf{x} contains all retrieved parameters, including the real refractive index of the particles n_p . The vector \mathbf{b} consists of quantities that influence the measurement and are known to some level of accuracy, but are not retrieved quantities.

After linearising about a reference state, \mathbf{x}_0 , Eq. (18) becomes:

$$\mathbf{y} - \mathbf{F}(\mathbf{x}_0, \mathbf{b}) = \mathbf{K}(\mathbf{x} - \mathbf{x}_0) + \boldsymbol{\epsilon}, \quad (19)$$

where \mathbf{K} is the Jacobian defined by $K_{ij} = \partial F_i(\mathbf{x}) / \partial x_j$, corresponding to the partial derivative of a forward model element with respect to a state vector element. The dimensions of \mathbf{K} are $m \times n$.

When a retrieval is performed on the experimental data, a best estimate of the state, $\hat{\mathbf{x}}$, is produced:

$$\hat{\mathbf{x}} = \mathbf{R}(\mathbf{y}, \mathbf{b}), \quad (20)$$

and after linearising this becomes:

$$\hat{\mathbf{x}} = \mathbf{G}\mathbf{y}, \quad (21)$$

where \mathbf{G} is the gain matrix and represents the sensitivity of the retrieved state to changes in the measurement vector, $\mathbf{G} = \partial \mathbf{R} / \partial \mathbf{y}$.

A least squares retrieval weighted by measurement error was performed on experimental data to determine the best estimate of the state, $\hat{\mathbf{x}}$. The minimised function was therefore:

$$(\mathbf{y} - \mathbf{K}\mathbf{x})^T \mathbf{S}_\epsilon^{-1} (\mathbf{y} - \mathbf{K}\mathbf{x}), \quad (22)$$

where \mathbf{S}_ϵ is the measurement error covariance matrix, defined by $S_{ij} = \langle \epsilon_i \epsilon_j \rangle$, with ϵ_i being the error associated with the i^{th} measurement. The gain matrix for this type of retrieval takes the form:

$$\mathbf{G} = (\mathbf{K}^T \mathbf{S}_\epsilon^{-1} \mathbf{K}) \mathbf{K}^T \mathbf{S}_\epsilon^{-1}. \quad (23)$$

The propagated uncertainty in the retrieved state, \mathbf{S}_x , has two contributions. The first contribution, $\mathbf{G}\mathbf{S}_\epsilon\mathbf{G}^T$, results from the application of the retrieval to the measurement error. The second contribution, $\mathbf{G}\mathbf{K}_b\mathbf{S}_b\mathbf{K}_b^T\mathbf{G}^T$, results from errors associated with forward model parameters, with $\mathbf{K}_b = \partial \mathbf{F} / \partial \mathbf{b}$ being the sensitivity of the forward model to forward model parameters. The combined uncertainty associated with the retrieved state is:

$$\mathbf{S}_x = \mathbf{G}\mathbf{S}_\epsilon\mathbf{G}^T + \mathbf{G}\mathbf{K}_b\mathbf{S}_b\mathbf{K}_b^T\mathbf{G}^T. \quad (24)$$

4.2. Modelling error

Often simplifying assumptions are made because the real physics is either not known or cannot be modelled accurately. The modelling error is given by:

$$\mathbf{G}\Delta\mathbf{f} = \mathbf{G} [\mathbf{f}(\mathbf{x}, \mathbf{b}, \mathbf{b}') - \mathbf{F}(\mathbf{x}, \mathbf{b})], \quad (25)$$

where \mathbf{f} contains the correct physics and \mathbf{b}' contains additional model parameters.

4.3. Computing sensitivities

In order to evaluate the uncertainty in retrieved quantities the forward model sensitivities, \mathbf{K} and \mathbf{K}_b , must be computed. These are simply linearisations of the forward model — Eq. (19) — and therefore vary as a function of the state vector \mathbf{x} .

In order to compute these sensitivities, one element of the state vector was perturbed by a fraction of 10^{-5} about a reference state, \mathbf{x}_0 . The forward model was then applied to compute the resulting perturbed measurement vector. The sensitivity derivative could then be calculated. By repeating for each element of the state vector, consecutive columns of the Jacobian, $K_{ij}(\mathbf{x}_0) = \partial F_i(\mathbf{x}_0) / \partial x_j$, were computed.

In addition to computing the propagated uncertainties at this reference state, it is also useful to investigate how the propagated uncertainties vary with position in state space (or assumed

model parameter space). Of particular interest is how these uncertainties vary with particle refractive index, and also with particle radius. For example, in order to investigate how the propagated uncertainties vary with particle refractive index, n_p , requires recalculation of the Jacobian over the desired range of n_p , whilst keeping the remaining parameters of the reference state fixed.

4.4. Sensitivity analysis of the monodisperse model and the polystyrene latex test particle retrieval

The analysis presented here is tailored to the type of retrieval performed on the polystyrene latex test particles. The reference state \mathbf{x}_0 was taken as the retrieved state from the retrieval on reflectivity data from a polystyrene latex sample with a measured volume filling fraction of $f = 6.70\%$. In the polystyrene particle retrievals the monodisperse model was used (the particles were manufactured to be monodisperse, with a coefficient of variation in size of $\leq 3\%$ quoted by the manufacturer). The state vector took the form $\mathbf{x} = (n_p, n_m)$. The parameter n_m was retrieved rather than fixed at the value of the refractive index of distilled water, because the presence of the polymer dispersant in the distilled water likely affects its refractive index. The volume filling fraction, f , which had been measured with an uncertainty of 5% was fixed at its measured value in the retrieval and thus formed an element in the vector of assumed model parameters; additional assumed model parameters were such that $\mathbf{b} = (f, a, \lambda)$.

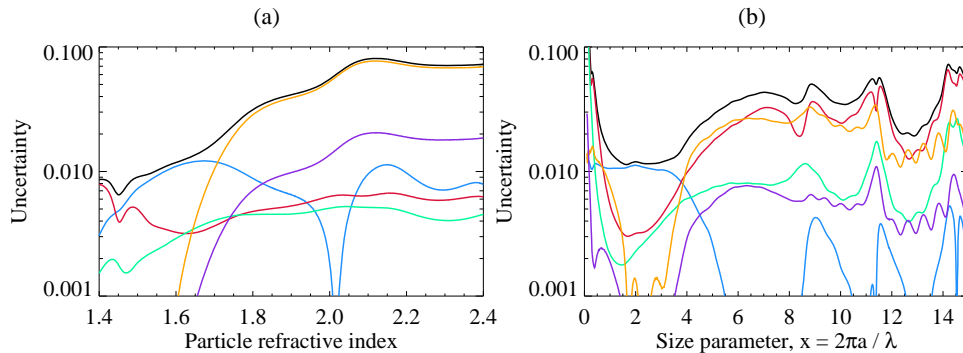


Fig. 5. The contributions to uncertainty in the retrieval of real refractive index for a monodisperse system plotted against (a) real refractive index and (b) size parameter. The contributions to the uncertainty and the combined uncertainty are shown: — volume filling fraction, — incidence angle, — laser power, — particle radius, — laser wavelength and — combined uncertainty. Uncertainty resulting from assuming non-absorbing particles was less than 0.001. The reference state was taken to be the retrieved state for a polystyrene latex sample with a measured volume filling fraction $f = 6.70\%$.

Figure 5 summarises the contributions to the combined uncertainty in the retrieval of real refractive index resulting from measurement uncertainties and uncertainties associated with assumed model parameters. The plots show how these error contributions vary (about the reference state) with particle refractive index and with size parameter — Figs. 5(a) and 5(b), respectively.

Table 1 sets out the contributions to propagated uncertainty at the reference state: the $f = 6.70\%$ retrieval result. It can be seen that the 5% uncertainty associated with the measured volume filling fraction contributes to the largest uncertainty in the retrieved real refractive index.

The uncertainty from assuming non-absorbing particles was calculated as follows. We can then take the imaginary particle refractive index to be zero, $k_p = 0$, providing we assign a parameter error comparable to the true magnitude of k_p . Xiaoyon *et al.* [40] found k_p for polystyrene

to be less than 0.001 for $\lambda < 800$ nm. The contribution to the propagated uncertainty is then given by $\mathbf{G}\mathbf{K}_b\mathbf{S}_b\mathbf{K}_b^T\mathbf{G}^T$, as detailed in Eq. (24), assuming a parameter error in k_p of 0.001. The resulting propagated uncertainty in the retrieval of n_p was found to be less than 0.001 for all values of x and n_p investigated.

In theory there is no restriction on including the imaginary refractive index of the particles in the forward model. However, the value of the imaginary refractive index of polystyrene in the visible is very low and has very little effect on the reflectivity of the system or the retrieval of n_p , as demonstrated by the results of this sensitivity analysis.

Table 1. Summary of contributions to the propagated uncertainty in the retrieval of n_p for the retrieval using the monodisperse CSM performed on the polystyrene latex particle reflectivity data. The values shown were calculated at the retrieved state of the $f = 6.70\%$ scan.

Error Term, e	σ_e	Propagated uncertainty, $\left \frac{\delta n_p}{\delta e} \right \sigma_e$
Volume filling fraction, f	5 %	0.01070
Incidence angle, θ_i	0.05°	0.00331
Laser power, LP	1 %	0.00279
Particle radius, a	3 %	0.00039
Non-absorbing assumption		0.00004
Laser wavelength, λ	5 nm	0.00001
Combined uncertainty		0.01154

4.5. Sensitivity analysis for the polydisperse model and the sand and ash retrievals

This analysis is tailored to the type of retrieval performed on the sand and the volcanic ash samples. The polydisperse model, taking into account the interface region using a 50 slab system, was applied to experimental reflectivity data from these samples. A log-normal distribution was assumed, controlled by the median radius, a_0 , and geometric standard deviation, S . For these retrievals the state vector took the form $\mathbf{x} = (n_p, n_m, f, a_0, S)$, whilst the assumed model parameter vector had the form $\mathbf{b} = (\lambda)$. The reference state \mathbf{x}_0 was taken to be the retrieved state for a retrieval performed on sand reflectance data in which the retrieved volume filling fraction was $f = 5.01\%$.

Figure 6 summarises the error contributions in the retrieval of real refractive index as a function of particle refractive index and size parameter — Fig. 6(a) and Fig. 6(b), respectively. The size parameter is defined in terms of the median radius of the log-normal distribution: $x = 2\pi a_0/\lambda$. It can be seen from Fig. 6(b) that the minimum for combined uncertainty occurs for a size parameter of approximately 1.9, which for a laser wavelength of 635 nm corresponds to a median radius of 190 nm.

Table 2 shows the values of propagated uncertainty in the retrieval of real refractive index from each of the error terms. The particular values shown in the table apply for the polydisperse retrieval, employing a 50 slab interface region, performed on a sand sample with a retrieved volume filling fraction of $f = 5.01\%$ (see Table 4 for the full state vector). It can be seen that the largest error terms come from uncertainty in the measured incidence angles at which the reflectivity detector readings are made, and uncertainty in the laser power.

The uncertainty from assuming non-absorbing particles was calculated using a method identical to that outlined above for the monodisperse case. The imaginary particle refractive index was fixed at $k_p = 0$ and assigned a parameter uncertainty of 0.001 — Ball *et al.* [22] measured

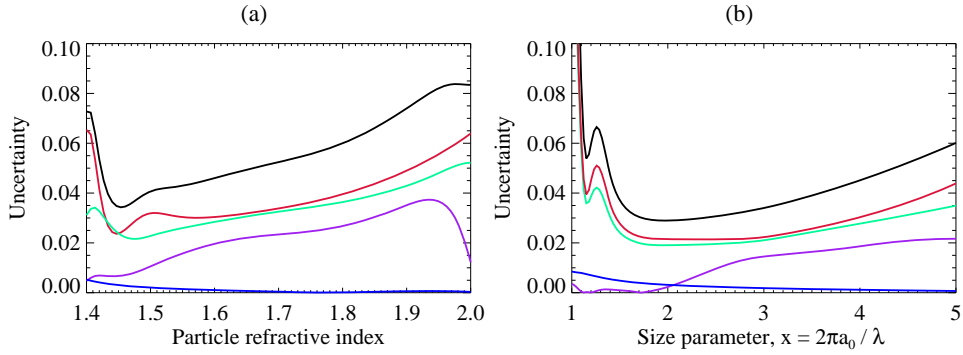


Fig. 6. The contributions to uncertainty in the retrieval of real refractive index for a polydisperse distribution taking into account the interface region using a 50 slab system: — incidence angle, — laser power, — non-spherical effects, — non-absorbing assumption and — combined uncertainty. The reference state was taken to be the retrieved state for the sand retrieval with a retrieved volume filling fraction of $f = 5.01\%$.

Table 2. Summary of the contributions to the propagated uncertainty in the retrieval of n_p for the polydisperse model taking into account the interface region using a 50 slab system. The reference state was taken to be the retrieved state for the sand retrieval with a retrieved volume filling fraction of $f = 5.01\%$.

Error Term, e	σ_e	Propagated uncertainty, $\left \frac{\delta n_p}{\delta e} \right \sigma_e$
Incidence angle, θ_i	0.05°	0.0301
Laser power, LP	1 %	0.0276
Non-spherical effects		0.0185
Non-absorbing assumption		0.0012
Laser wavelength, λ	5 nm	0.0001
Combined uncertainty		0.0449

the imaginary refractive index of Eyjafjallajökull ash to be 0.000850 ± 0.00069 at 650 nm. The propagated uncertainty was then calculated according to Eq. (24). As can be seen in Fig. 6 and Table 2 the forward model sensitivity to k_p is small.

The modelling error associated with assuming spherical particles (and therefore Mie scattering) was estimated. T -matrix scattering code, described in [34] Mishchenko *et al.*, was used to calculate the configurationally averaged scattering amplitude functions, S_1 and S_2 , for randomly orientated spheroids with an aspect ratio of 1.5 — an average aspect ratio of 1.47 ± 0.30 for Eyjafjallajökull ash was found in [22]. The forward model result using these non-spherical scattering amplitude functions was subtracted from the forward model result using Mie scattering amplitude functions to give Δf . The gain matrix was then applied to compute the propagated uncertainty, according to Eq. (25).

5. Results

5.1. Monodisperse polystyrene latex spheres

The monodisperse CSM was used within a least squares retrieval weighted by measurement errors — see Eq. (22) — to retrieve the state vector $\mathbf{x} = (n_p, n_m)$ from the experimental reflectivity scans on the suspensions of polystyrene latex particles with varying volume filling

fractions in distilled water. The refractive index of the suspension medium n_m was retrieved because of the additional polymer dispersant present, which is likely to alter slightly the refractive index of the distilled water used to suspend the polystyrene particles. The volume filling fraction for each scan was fixed at its measured value in the retrieval. The vector of assumed model parameters had the form $\mathbf{b} = (f, a, \lambda)$, with the particle radius fixed at $a = 260$ nm and the incidence wavelength fixed at $\lambda = 635$ nm.

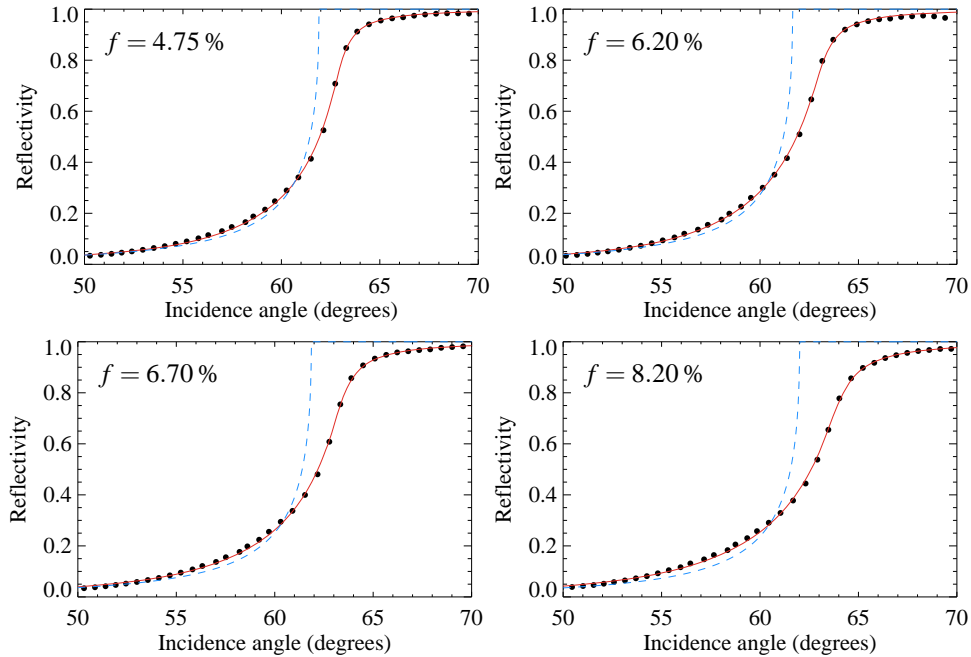


Fig. 7. Reflectivity scans for polystyrene latex spheres in distilled water at differing volume filling fractions. Shown are the fitted reflectivity curve — using the monodisperse CSM and the Fresnel reflectivity curve - - - for a suspension medium containing no scatterers with a refractive index equal to the retrieved value of n_m .

Figure 7 shows the experimental data points at different volume filling fractions. The fitted reflectivity curves are shown in red. The Fresnel reflectivity for a homogeneous medium (containing no scatterers) with a refractive index equal to the retrieved value of n_m is shown as a dashed blue line.

Table 3 summarises the retrieval results for the polystyrene latex sphere suspensions of varying volume filling fraction. The weighted mean refractive index from the polystyrene scans is $\langle n_p \rangle = 1.5931 \pm 0.0052$ at 635 nm. This compares to the value for the refractive index of polystyrene of 1.5870 ± 0.001 at 635 nm according to [41], Kasarova *et al.*

5.2. Polydisperse sand sample

The number of slabs, N , used to model the transition region was determined by analysing reflectivity curves, produced by the forward model, increasing N in increments of 5 (with all other parameters fixed). It was found that the reflectivity curves rapidly converged. The improvement in increasing the number of slabs beyond 50 was small; the maximum difference in reflectivity for $N = 50$ compared to $N = 100$ was less than 0.1% (i.e. less than 10% of the laser power uncertainty).

The polydisperse CSM using a 50 slab system to model the interface region was employed in

Table 3. Summary of polystyrene latex sphere retrieval results using the monodisperse CSM.

Measured f (%)	Retrieved n_p	Retrieved n_m
4.75	1.6045 ± 0.0127	1.3364
6.20	1.5932 ± 0.0120	1.3337
6.70	1.5933 ± 0.0117	1.3359
8.27	1.5868 ± 0.0111	1.3379
10.36	1.5906 ± 0.0109	1.3398

the retrievals. The particle size distribution was assumed to be log-normal. The median radius a_0 and width parameter S were retrieved. The state vector for the retrieval took the form $\mathbf{x} = (n_p, n_m, f, a_0, S)$ and the parameter vector was $\mathbf{b} = (\lambda)$. A least squares retrieval weighted by measurements errors was employed. The suspension medium refractive index was included as a retrieved parameter, as it is possible that the sand sample has a small component of soluble material which may alter slightly the refractive index of the distilled water used to suspend the sand.

Table 4. Summary of the retrieval results on the sand sample.

n_p	n_m	f (%)	a_0 (nm)	S
1.6099 ± 0.0586	1.3338	3.66	424.6	1.145
1.6211 ± 0.0553	1.3317	4.41	417.0	1.146
1.5837 ± 0.0449	1.3323	5.01	402.1	1.127
1.5603 ± 0.0446	1.3339	5.56	450.2	1.108
1.5530 ± 0.0551	1.3353	6.06	432.8	1.183
1.5370 ± 0.0548	1.3310	6.08	435.7	1.184

Table 4 summarises the retrieval results for the sand sample. The mean refractive index for the sand from the 6 scans is $\langle n_p \rangle = 1.576 \pm 0.021$ at 635 nm. This compares to values measured using the Becke line technique of 1.566 ± 0.01 at 546.1 nm and 1.560 ± 0.01 at 650 nm.

5.3. Polydisperse volcanic ash sample

The same type of retrieval, outlined in section 5.2, was used for the volcanic ash reflectivity data. As with the sand retrievals, the suspension medium refractive index was included as a retrieved parameter because the volcanic ash is likely to have a small soluble component that may alter slightly the refractive index of the distilled water used to suspend the ash.

Table 5 summarises the retrieval results for the volcanic ash samples. Sample A and sample B were produced from the same bulk ash sample, but were left to settle for 12 hours and 24 hours respectively for the sedimentation process. Table 5 shows a clear variation in the retrieved log-normal size distribution parameters between the two samples.

The mean refractive index from the 6 scans on volcanic ash was $\langle n_p \rangle = 1.553 \pm 0.024$ at 635 nm. The same volcanic ash sample's refractive index was measured using the Becke line method and was found to be 1.546 ± 0.01 at 546.1 nm and 1.548 ± 0.01 at 650 nm. The Becke line method is only applicable to particles with a radius larger than approximately 500 nm, as determined by the resolvable limit of the optical microscope used for the technique. Comparison with the result obtained using the reflectance measurements, indicates no evidence of a

Table 5. Summary of the retrieval results on samples made from an Icelandic volcanic ash. Sample A underwent a 12 hour sedimentation process whilst for Sample B the period was 24 hours.

Sample	n_p	n_m	f (%)	a_0 (nm)	S
A	1.5684 ± 0.0710	1.3346	3.18	314.5	1.278
A	1.5597 ± 0.0523	1.3345	8.23	314.1	1.285
A	1.5269 ± 0.0549	1.3358	9.19	323.8	1.313
B	1.5561 ± 0.0573	1.3334	5.97	208.2	1.503
B	1.5535 ± 0.0596	1.3369	9.48	241.6	1.426
B	1.5308 ± 0.0587	1.3366	10.66	255.1	1.411

variation in refractive index between the Becke line size regime and the size regime of the reflectance measurements (indicated by the retrieved modal radii in Table 5).

6. Conclusions

This paper determines the accuracy in retrieving the real refractive index, at visible wavelengths, of submicron monodisperse or polydisperse aerosol particles from angular reflectivity measurements of a dilute colloidal suspension of the aerosol. The coherent scattering model [26] has been applied to model the reflectivity from the colloidal suspension. An extension of this model for polydisperse suspensions, similar to that in [33], is presented which properly accounts for the modified particle size distribution close to the medium-to-colloid interface. The modified distribution occurs because a particle of radius a cannot approach closer than a to the interface, resulting in an increase in the relative density of smaller particles as the interface is approached. A sensitivity analysis was performed on the monodisperse and polydisperse models, which determines how experimental uncertainties propagate into uncertainty associated with the retrieval of real refractive index.

Experimental reflectivity data, at a wavelength of 635 nm, were obtained for a monodisperse suspension of polystyrene latex spheres with a known refractive index, a polydisperse sand sample and a polydisperse sample of volcanic ash. The monodisperse CSM was used to retrieve the real refractive index of the polystyrene particles, and the value obtained agreed with the known value to within uncertainties predicted by the sensitivity analysis. Similarly, the polydisperse CSM, using a 50 slab interface transition region and assuming a lognormal size distribution, was used to retrieve the real refractive index from the reflectivity data obtained for the sand and ash samples. The retrieved refractive index for the sand and ash samples agreed, to within derived uncertainties, with values obtained using the Becke line method on the same samples. However, comparison of refractive indices obtained from the two techniques is complicated because they are sensitive to different particle size regimes. The advantage of the technique, presented in this paper, is its sensitivity to submicron particles (as demonstrated by the sensitivity analysis of section 4, and in particular Fig. 6(b)) whereas the Becke line technique is limited by the resolving ability of an optical microscope, typically to particles with a diameter $> 1 \mu\text{m}$.

In the forward model used to predict the reflectivity from the colloidal suspensions, spherical particles were assumed and therefore the Mie scattering amplitude functions used. However, volcanic ash particles are known to have irregular non-spherical shapes [23]. In principle, there is no reason why non-spherical scattering amplitude functions could not be used in the forward model replacing the assumed Mie scattering amplitude functions. By employing T -matrix code, we have included in the sensitivity analysis an estimate of the systematic uncertainty introduced

into the retrieval of real refractive index resulting from non-spherical scattering effects.

An area for possible improvement for retrieving the real refractive index of ash samples from this method would be to incorporate independent sizing measurements of the aerosol. In the retrievals performed on the reflectivity data from the polydisperse sand and ash samples, a lognormal distribution was assumed with a_0 and S being retrieved parameters. If accurate independent sizing data could be obtained for the submicron aerosol, their incorporation could significantly reduce uncertainties associated with the retrieval of real refractive index for polydisperse samples.

In conclusion we present a method for retrieving the real refractive index of submicron aerosol particles from near critical angle reflectivity measurements from a dilute colloid containing the aerosol. The technique has been successfully applied to monodisperse polystyrene latex spheres of radius 260 nm, a polydisperse sand sample and a polydisperse volcanic ash sample. In the future we aim to apply the method to a range of volcanic ash samples. Comparison of these results with those obtained using the Becke line method will allow any variation in real refractive index between submicron and particles larger than one micron to be investigated.

Acknowledgments

R.G.G. and D.M.P. acknowledge funding from the NERC VANAHEIM project NE/1015592/1 and the NERC SHIVA project NE/J023310/1. B.E.R. was funded by a NERC studentship NE/J500045/1. This study was funded as part of NERCs support of the National Centre for Earth Observation and the Centre for Observation and Modelling of Earthquakes, Volcanoes, and Tectonics.